



## Solvothermal sol-gel synthesis of TiO<sub>2</sub> cellulose nanocrystalline composites

Andrey Zdravkov, Maria Listratenko, Stanislav Gorbachev, Iraida Osovskaya,  
Andrei Kanaev, Nikolai Khimich

### ► To cite this version:

Andrey Zdravkov, Maria Listratenko, Stanislav Gorbachev, Iraida Osovskaya, Andrei Kanaev, et al.. Solvothermal sol-gel synthesis of TiO<sub>2</sub> cellulose nanocrystalline composites. Cellulose, 2021. hal-03092629

**HAL Id: hal-03092629**

**<https://hal.science/hal-03092629>**

Submitted on 2 Jan 2021

**HAL** is a multi-disciplinary open access archive for the deposit and dissemination of scientific research documents, whether they are published or not. The documents may come from teaching and research institutions in France or abroad, or from public or private research centers.

L'archive ouverte pluridisciplinaire **HAL**, est destinée au dépôt et à la diffusion de documents scientifiques de niveau recherche, publiés ou non, émanant des établissements d'enseignement et de recherche français ou étrangers, des laboratoires publics ou privés.

1 Andrey Zdravkov<sup>a</sup>, Maria Listratenko<sup>b</sup>, Stanislav Gorbachev<sup>c</sup>, Iraida Osovskaya<sup>c</sup>,  
2 Andrey Kanaev<sup>d</sup>, Nikolai Khimich<sup>b</sup>

3

# 4 **Solvothermal sol-gel synthesis of TiO<sub>2</sub>-** 5 **cellulose nanocrystalline composites**

6 *<sup>a</sup> Grebenshchikov Institute of Silicate Chemistry, Russian Academy of Sciences,*  
7 *Makarova emb. 2, 199034, St. Petersburg, Russian Federation*

8 *<sup>b</sup> Kirov Military Medical Academy, Akademika Lebedeva str. 6, 194044, St.*  
9 *Petersburg, Russian Federation*

10 *<sup>c</sup> St. Petersburg State University of Industrial Technology and Design the Higher*  
11 *School Of Technologies and Power Engineering, Ivana Chernykh str. 4, 198095,*  
12 *St. Petersburg, Russian Federation*

13 *<sup>d</sup> Laboratoire des Science des Procédés et des Matériaux, CNRS, Université*  
14 *Sorbonne Paris Nord, 93430, Villetaneuse, France*

15

16

17

18

19

20

21

22

23

24

25

26

27

28

29

30

31

32

33

## 34 **Abstract**

35 Due to its unique supramolecular structure, cellulose is widely used as a template agent, ensuring  
36 an easy structuring of anatase  $\text{TiO}_2$  particles with subsequent release after the organics burning.  
37 This work is devoted to the synthesis of microcrystalline cellulose- $\text{TiO}_2$  (MCC- $\text{TiO}_2$ ) composite  
38 photocatalyst by preserving the intermediate organic-inorganic structures. A series of the MCC-  
39  $\text{TiO}_2$  materials were prepared via solvothermal sol-gel method in n-decane and caproic acid  
40 solvents and characterized by X-ray diffraction, transmission electron microscopy, IR  
41 spectroscopy,  $^1\text{H}$  NMR and TG/DSC methods. The photocatalytic activity of the prepared  
42 materials was evaluated by the decomposition of formic acid in aqueous solutions. The composites  
43 failed to be formed in n-decane, while in caproic acid, acting as solvent and reagent, anatase  $\text{TiO}_2$   
44 nanoparticles were formed onto the crystalline domains of cellulose, tightly fixed due to covalent  
45 Ti-O-C bonds. The materials formed in caproic acid showed a higher photocatalytic activity,  
46 explained by a complementarity of the organic and inorganic components. The specific activity  
47 (normalized on  $\text{TiO}_2$  mass) of best synthesized composite materials was almost twice higher than  
48 that of Aeroxide P25  $\text{TiO}_2$  reference photocatalyst.

## 49 **Keywords**

50 Microcrystalline cellulose-titania composite; solvothermal synthesis; sol-gel

## 51    **Introduction**

52    Among different semiconductors ( $\text{TiO}_2$ ,  $\text{WO}_3$ ,  $\text{Fe}_2\text{O}_3$ ,  $\text{SrTiO}_3$ ,  $\text{ZnO}$ , etc.) that can  
53    be used in photocatalytic process for degradation of organic pollutants,  $\text{TiO}_2$  has  
54    received a particular interest because of its high activity, chemical stability,  
55    relatively low cost and low toxicity [Mory 2005; Sharon et al. 2016; Tang et al.  
56    2018]. However, the research on the improved photocatalyst design is still under  
57    way. Between different approaches, composite materials can be an interesting  
58    solution capable affecting charge separation and trapping effectiveness and light  
59    absorption efficiency. A striking example of a two-component system of noble  
60    metal and semiconductor particles can be given [Zhang et al. 2013], which  
61    synergy is based on a Schottky junction and localized surface plasmon resonance.  
62    Excellent charge separation efficiency can also take place in composite or hybrid  
63    species including inorganic  $\text{TiO}_2$  and organic polymer components [Kuznetsov et  
64    al. 2009; Gorbovyi et al. 2011]. The synthesis of such materials has overcome  
65    numerous problems, related to the preparation of ensembles of freestanding  
66    particles, their uniform distribution free of aggregation, and link to the host  
67    polymer by strong covalent bonds.

68    Both inorganic (e.g. montmorillonite [Tieng et al. 2011]) and organic (e.g.  
69    polyamide-amine-epichlorohydrin [Wang et al. 2015], polylactide [Kaseem et al.  
70    2019]) polymers can be taken as complementary components of photocatalytic  
71    materials. At the same time, use of natural biopolymer cellulose could be a  
72    particularly attractive solution [Dette et al. 2014; Filippo et al. 2015; Sathasivam  
73    et al. 2015; He et al. 2016; Butman et al. 2018; Garusinghe et al. 2018;  
74    Rahmawati et al. 2017; Wittmar et al. 2015; Oliveira et al. 2017; Shahrezaei et al.  
75    2017.; Melvin et al. 2019; Habibi et al. 2020]. Cellulose does not absorb in the  
76    UV-visible spectral range [Sirvio et al. 2016] and cannot screen action spectrum  
77    of the photoactive  $\text{TiO}_2$  component. A very interesting supramolecular structure  
78    and multilevel structural organization of this polymer [Farag et al. 2017] explains  
79    its wide use as a template agent [Ioelovich 2014; Lu et al. 2013; Wang et al. 2016;  
80    Kayaalp et al. 2014; Xiao et al. 2017; Postnova et al. 2015; Zlotski et al. 2017;  
81    Shevtsova et al. 2018; Brandes et al. 2016], ensuring an easy structuring of  
82    anatase  $\text{TiO}_2$  particles. The thermal post-treatment performed in the related studies  
83    has resulted in a burnout of the organic component with subsequent formation of  
84    anatase nanoparticles with the shape and size control, exhibiting photocatalytic

85 activity [Postnova et al. 2015]. Naturally, cellulose degrades in these conditions  
86 leading to the decomposition of the intermediate structures. Attempts to preserve  
87 the organic component in the final photocatalyst are rare [Galkina et al. 2014;  
88 Khalid et al. 2017; Luo et al. 2014; Morawski et al. 2013; Melvin et al. 2019; Sun  
89 et al. 2010]. The synthesis by decomposition of titanium isopropoxide in ethanol  
90 media together with wood cellulose fibers in the microwave-assisted solvothermal  
91 process has been reported by Cardoso et al. [Cardoso et al. 2018] and the  
92 mechanism of the nucleation and growth of TiO<sub>2</sub> nanoparticles on cellulose fibers  
93 has been depicted. Although photocatalytic applications were suggested, no  
94 evaluation of the material activity has been presented in this study. The  
95 photocatalyst preparation via low-temperature sol-gel method has been reported  
96 by Morshed et al. [Morshed et al. 2020] and its activity on methylene blue dye  
97 decomposition in aqueous solution (pH=6) under UV light resulted in the first  
98 order kinetics with rate constant of 0.188 1/min. The material has shown a good  
99 stability with negligible deactivation after 5 recycling. Very recently, Li et al. [Li

et al. 2020] have realized a controlled synthesis of TiO<sub>2</sub>-cellulose nanocomposites via biotemplate method and assigned an enhanced photocatalytic activity to the ligand-to-metal charge transfer complex at the interface between the components. In this study, the material activity has been evaluated on Cr(VI) reduction in particular acid conditions at pH=3 in the visible spectral range of  $\lambda \geq 420$  nm and compared with P25 TiO<sub>2</sub>, which is a well-known UV-sensible reference photocatalyst offering a weak absorbance in acid media. Because of this, this activity concerned participation of intraband defect levels and not to the common photocatalytic mechanism involving the interband electronic transitions. Many points, including the component mass ratio and type of binding between the constituting organic and inorganic components have to be explored in order to understand potentiality of the TiO<sub>2</sub>-cellulose nanocomposites in photocatalysis. In this work, we developed a method for synthesis of a composite material, consisting of TiO<sub>2</sub> nanoparticles strongly bound to microcrystalline cellulose and possessing an enhanced photocatalytic activity owing to a specific participation of both constituting components.

## Experimental

Caproic acid (Aldrich, 98%), n-decane (Aldrich, 99%), titanium tetraisopropoxide (TTIP, Aldrich, 97%) and microcrystalline cellulose (MCC, Aldrich, 10 wt. % H<sub>2</sub>O) were used in the synthesis. Caproic acid and n-decane were additionally dried over molecular sieves (Merck). To obtain anhydrous cellulose if necessary, the commercial MCC was dried at 110°C in a vacuum (0.1 mm Hg). All manipulations preceding the heat treatment in an autoclave were performed in a glove box filled with dry argon. In a typical experiment, TTIP was dissolved in 15 mL of caproic acid (or in 15 mL of n-decane), and 1 g of MCC was added. After a thorough mixing, the reaction mixture was placed in a Teflon liner of a steel autoclave (internal volume 50 mL) under argon and heated to 200°C. The samples were separated on a Schott filter, washed successively with decane, petroleum ether, and alcohol and dried thereafter without any contact with atmospheric moisture. The samples were examined by IR spectroscopy (FSM-2201 device) and X-ray diffraction (Rigaku SmartLab 3 diffractometer, CuK $\alpha$  radiation,  $\lambda = 1.54051$  Å) methods. The particle crystalline size was determined from the (101) diffraction

line width using the Scherrer equation. The crystallinity index (CrI) was calculated as the ratio of the highest peak (crystalline peak  $I_{200}$ ) to that of the minimum ( $I_{am}$ ) (Segal et al. 1959) between the (110) and (102)/(012) peaks at about  $2\theta = 18.5^\circ$  (French 2014). Examination of each of the sample (MCC, TiC(1-4)) results in curves whose measured heights above a base line at  $2\theta = 18.5^\circ$  and  $22.8^\circ$  gave the value  $I_{am}$  and  $I_{200}$  respectively.

$$CrI = \frac{I_{200} - I_{am}}{I_{200}}$$

The specific surface area was estimated by the BET method, pore volume, and average pore size were estimated by the BJH method from the nitrogen adsorption/desorption isotherms measured with Quantachrome NOVA 1200e instrument. For measurements samples were treated at  $110^\circ\text{C}$  in vacuum ( $<0.1$  mmHg) for 2 h. The transmission electron micrographs (TEM) were taken with a JEOL JEM-100C device, after preparing the analytic samples in chloroform.  $^1\text{H}$  NMR spectra were recorded with JEOL ECX-400A instrument at 400 MHz, after preparing the analytic samples in benzene- $d_6$ . The UV-visible absorption spectra of the samples prepared were measured with SF-2000 spectrometer equipped with an integrating sphere. The thermal analysis was performed with Netzsch STA 429 device under dry argon gas atmosphere.

The photocatalytic activity of the materials prepared was evaluated by monitoring the decomposition of formic acid ( $pK_a = 3.75$ , initial concentration 0.35 mmol/l) in aqueous solution of a total volume 100 mL. Prior to UVA irradiation, every synthesized sample of 10 mg mass was dispersed during 10 min under ultrasound in 1 mL of water until a stable suspension of was formed. When using caproic acid, 1% KOH solution was taken instead of water, with the subsequent neutralization to pH 5. The photocatalytic medium was prepared under air flow in a dark under magnetic stirring for 30 min. The prepared suspensions were irradiated with a DRL-100 high-pressure mercury lamp under continuous magnetic stirring. The lamp emits in the UV-visible range with the most intense UVA line at  $\sim 365$  nm (90% of the lamp intensity). The reaction solutions were periodically analyzed, and the initial ( $C_0$ ,  $t=0$ ) and current ( $C$ ,  $t>0$ ) formic acid concentrations were calculated from the solution acidity. The solution acidity was determined with an I-510 ionometric converter with an accuracy of  $\pm 0.01$  pH unit. Aeroxide P25  $\text{TiO}_2$  (Sigma-Aldrich) of a mean particle size 21 nm and specific surface area 35-65  $\text{m}^2/\text{g}$  (BET) was used as a reference sample.

To evaluate the effect of the mass exchange on the rate of photocatalytic decomposition of formic acid, the stirring rate of the photocatalytic medium was varied from 200 to 800 rpm. These measurements revealed no appreciable influence of stirring on the decomposition rate, which permits to conclude that the mass transport was not a limiting stage in our experimental conditions and that the decomposition rate depends mostly on the material activity.

A list of the synthesized samples along with their preparation conditions are summarized in Table 1. Samples indicated as TiD and TiC were respectively prepared in decane and in caproic acid and samples TiDH<sub>2</sub>O and TiO<sub>2</sub>D<sub>2</sub> were prepared in decane from commercial cellulose. The synthesis of all samples was performed at 200°C. The details of preparation given in Table 1.

**Table 1.** Synthesis conditions and photocatalytic rate constant (R) of TiO<sub>2</sub>–MCC composites.

Sample	Solvent	Reaction time (h)	TiO <sub>2</sub> content (g)**	R (h <sup>-1</sup> )***	Error bars +/-
TiDH <sub>2</sub> O	n-decane	8	0.27	0.100	0.005
TiD1	n-decane	8	0.27	0.153	0.006
TiD2	n-decane	15	0.27	0.195	0.008
TiD3	n-decane	30	0.27	0.223	0.008
TiO <sub>2</sub> D <sub>2</sub> *	n-decane	15	0.27	0.273	0.017
TiC1	caproic acid	8	0.05	0.278	0.011
TiC2	caproic acid	8	0.13	0.520	0.020
TiC3	caproic acid	8	0.27	0.600	0.033
TiC4	caproic acid	8	0.54	0.654	0.036
TiC5	caproic acid	2	0.27	0.408	0.011
TiC6	caproic acid	4	0.27	0.458	0.012
TiO <sub>2</sub> C <sub>3</sub> *	caproic acid	8	0.27	0.343	0.010
TiO <sub>2</sub> P25				0.732	0.040

\* Samples prepared with an additional calcination at 500°C for 2 h.

\*\* TiO<sub>2</sub> content corresponds to the initial TTIP amount mixed with 1 g MCC.

\*\*\* Corresponds to the first order kinetics. Tests were performed with 10 mg powders.



## Results and Discussion

Our attempts failed to prepare anatase  $\text{TiO}_2$ -MCC composites using the commercial MCC. This is apparently due to the fact that hygroscopic cellulose contains about 10 wt% of water. The X-ray diffraction analysis of  $\text{TiDH}_2\text{O}$  sample (Fig. 1) showed that nanosized anatase is formed when performing the synthesis in TTIP–MCC (commercial)–*n*-decane system but anatase and MCC behave as the independent components. In fact, TEM micrograph in Fig. 2 clearly shows that majority of anatase  $\text{TiO}_2$  crystallites were separated from MCC grains, forming a mixture of a priori non-interacting particles ( $\text{TiDH}_2\text{O}$ ). An increase in the cellulose grain size may be attributed to a partial grains sintering. In this case, one cannot expect any synergy revealed by the material components in the photocatalytic process.

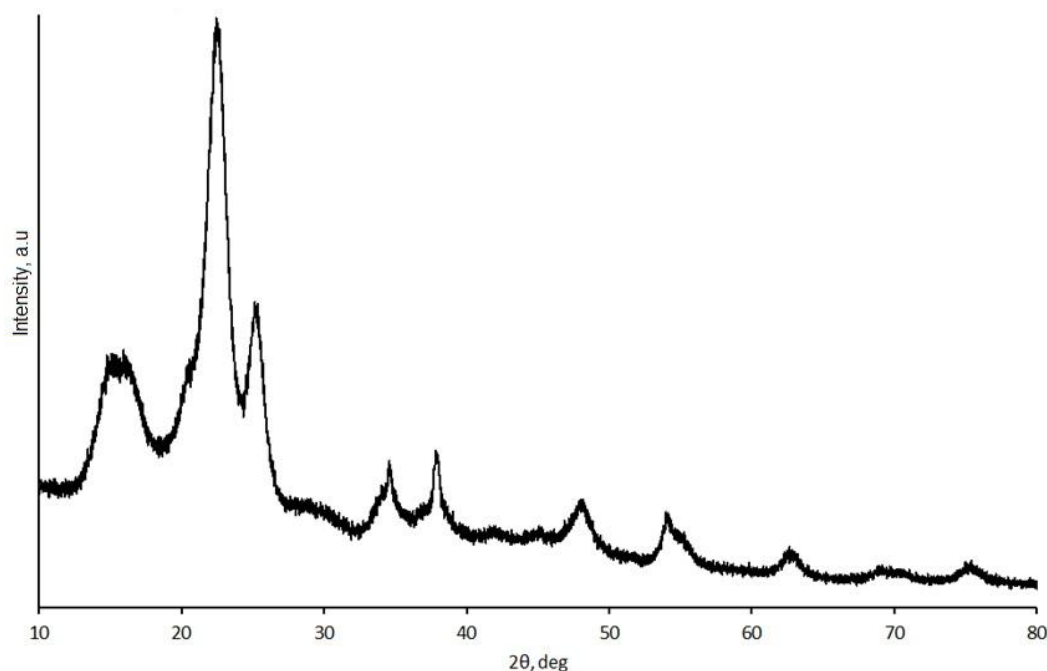
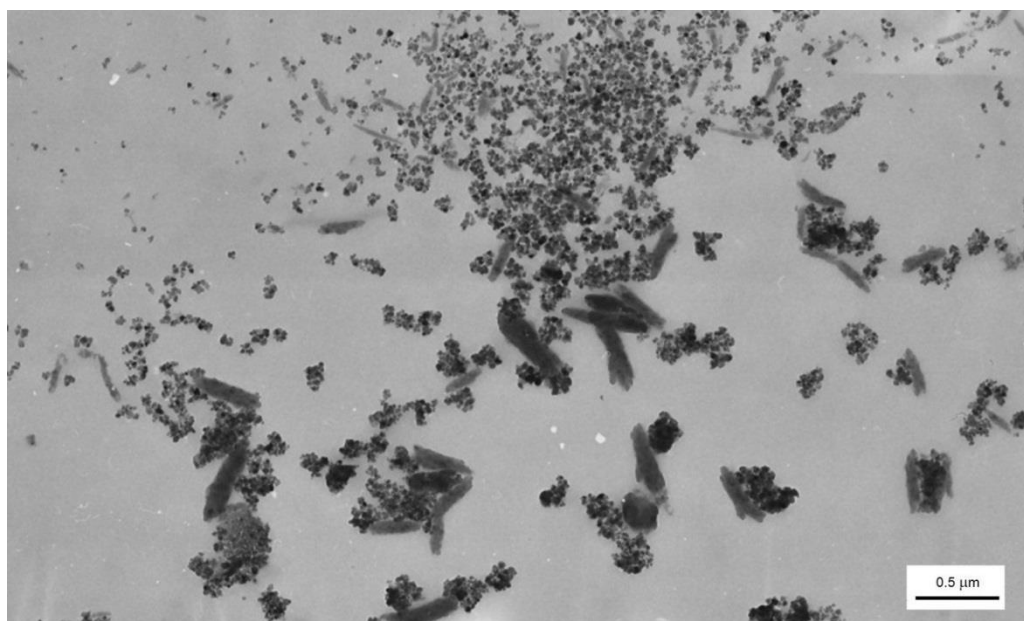


**Figure 1.** X-ray diffraction data of  $\text{TiDH}_2\text{O}$  sample.



198

199 **Figure 2.** TEM micrograph of TiDH<sub>2</sub>O sample.

200

201 The reaction of TTIP with anhydrous MCC in n-decane is rather slow, as  
202 confirmed by the fact that Bragg reflections of anatase TiO<sub>2</sub> did not significantly  
203 show up in X-ray diffraction pattern of TiD1 sample (Fig. 3), even after 8 hours of  
204 the reaction runtime, which pattern is almost identical to that of pure cellulose  
205 (MCC).

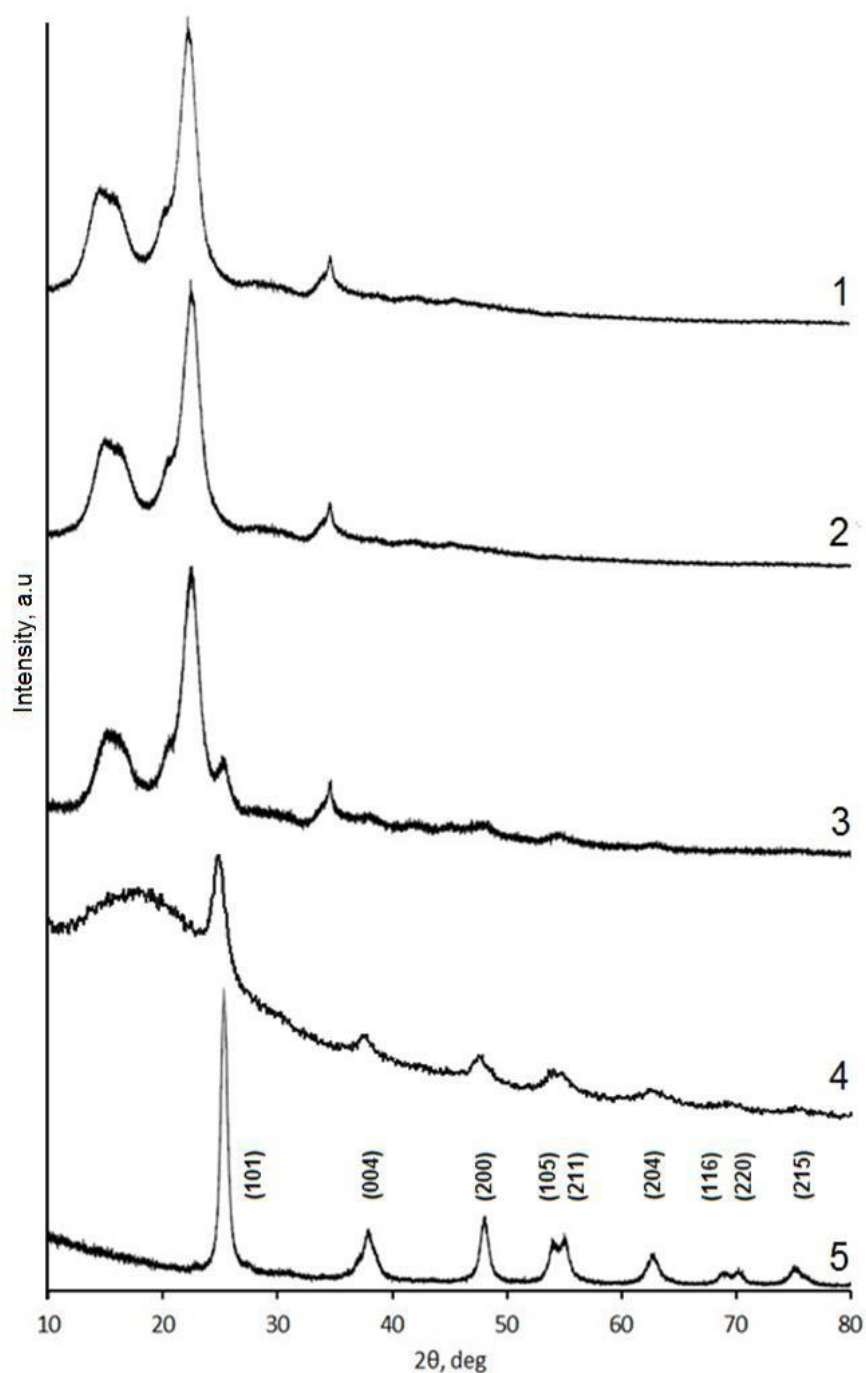


**Figure 3.** X-ray diffraction data of MCC (1), TiD1 (2), TiD2 (3), TiD3 (4) and TiO<sub>2</sub>D2 (5).

The titania attachment to the cellulose surface begins in these conditions through the condensation reactions between the most active hydroxy group of cellulose at C<sup>6</sup> carbon atom and OR- of Ti cation with the release of isopropyl alcohol (Fig. 4).

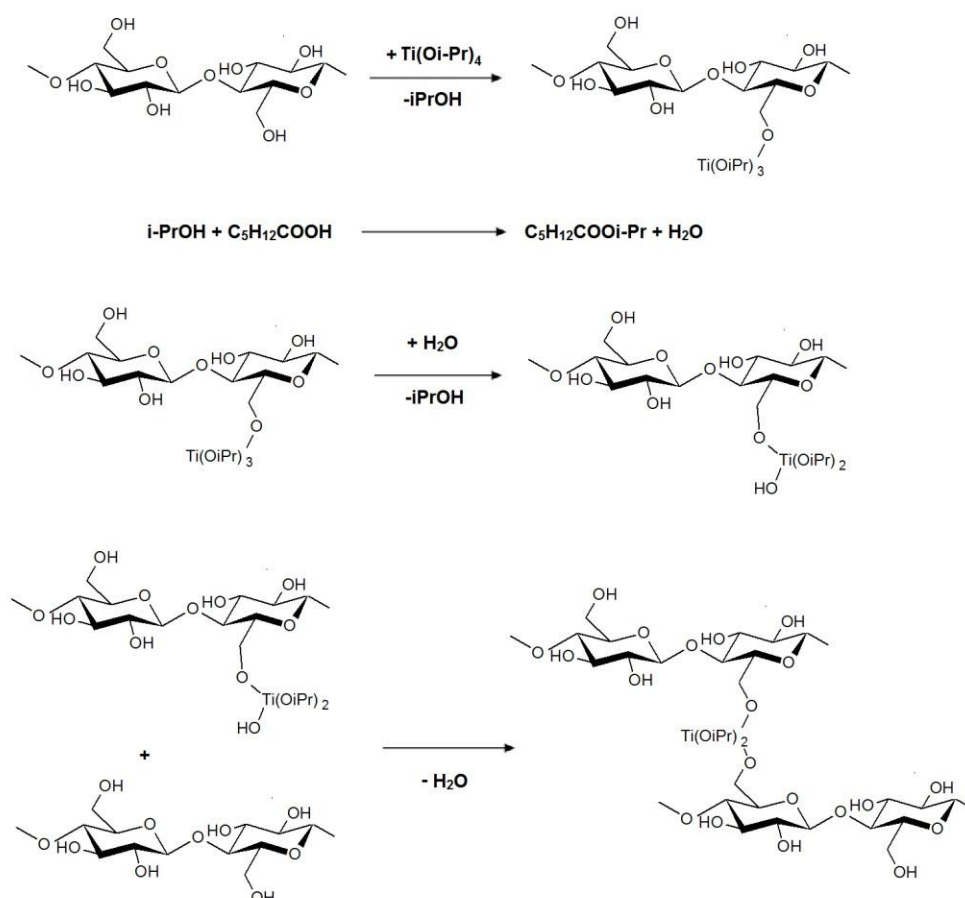
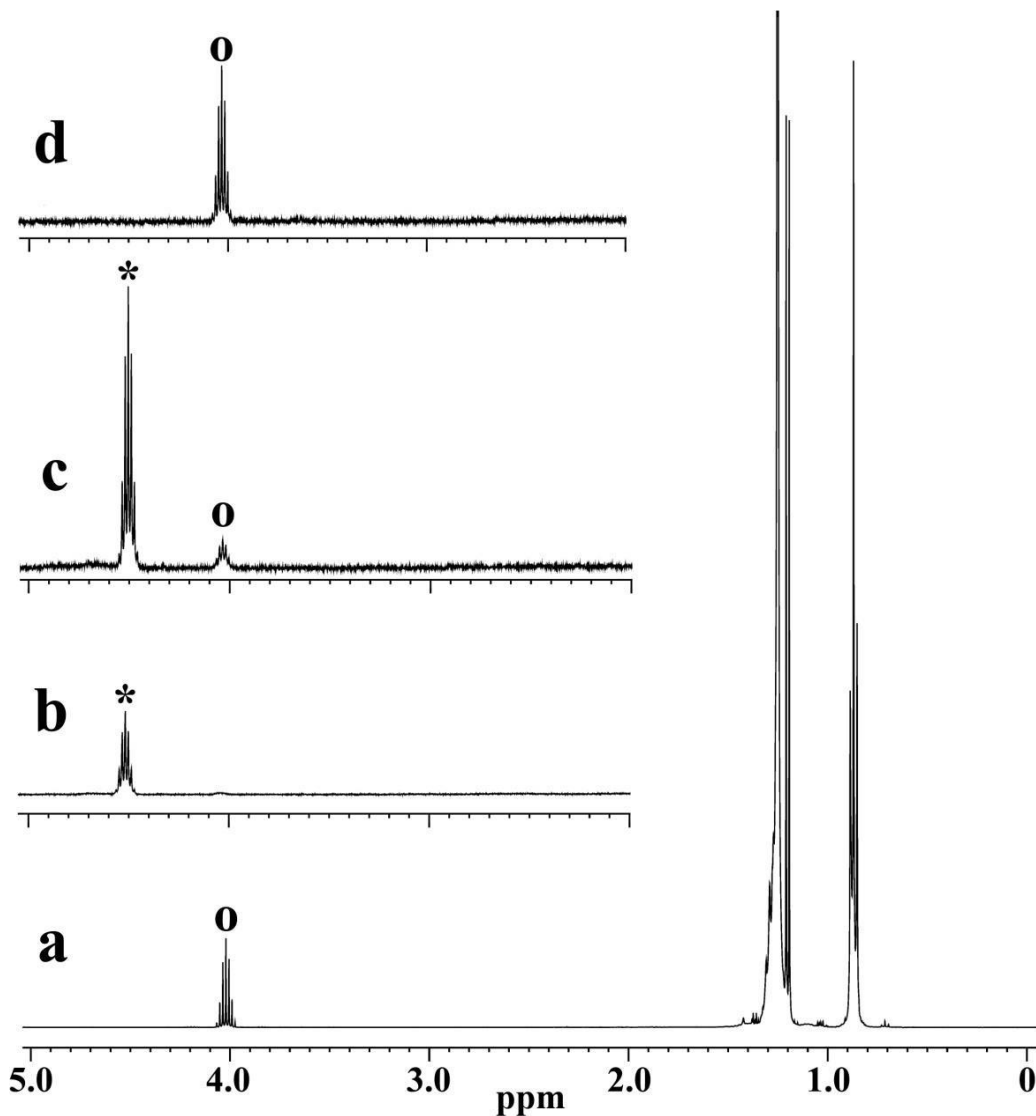


**Figure 4.** Tentative reaction scheme.

This process was confirmed by  $^1\text{H}$  NMR measurements shown in Fig. 5. Two solutions of TTIP and isopropyl alcohol in decane and reference samples were examined in this series. The signal of the decane proton was observed in all spectra at high fields ( $\delta < 1.5$  m.d). The proton of the secondary carbon atom in TTIP gives a septet at 4.50 ppm ( $J = 6.18$  Hz), and the relevant proton in isopropyl alcohol molecule gives a septet at 4.03 ppm ( $J = 6.11$ ). The solvothermal process leads to smearing of the septet, suggesting distortion symmetry of the substituents at the titanium atom when isopropyl alcohol appears. We notice that the control series performed without TTIP showed that MCC was stable in the experimental conditions with the weight loss of the material below 0.2% during 8 hours of the autoclave treatment. A noticeable amount of anatase  $\text{TiO}_2$  was only obtained after a heat treatment of the reaction mixture in the autoclave for a longer time (TiD2 and TiD3 samples) and/or higher temperature (TiO<sub>2</sub>D2 sample), as show X-ray diffraction patterns of in Fig. 3. However, cellulose underwent a gradual degradation in this case; this can be seen from

230 comparison of curves 2, 3 and 4, where reflexes of MCC continuously weakened  
 231 and disappeared.



232  
 233 **Figure 5.** <sup>1</sup>H NMR spectra of isopropyl alcohol in decane (a), TTIP in decane (b), reaction mixture  
 234 after 2 h (c), reaction mixture after 8 h (d).

235  
 236 In order to obtain a stable anatase TiO<sub>2</sub>-MCC composite, n-decane solvent, which  
 237 did not work, was replaced by caproic acid contributed to the synthesis as reagent  
 238 and solvent in the same time. In the caproic acid medium, water is released in situ,  
 239 and this fact allows the composite formation process to be controlled. This  
 240 mechanism has been previously studied in Ref. [Zdravkov et al. 2015]. Fig. 6  
 241 shows that the formation of the anatase structure occurs already in the first 2 hours  
 242 of the reaction and the formation of anatase TiO<sub>2</sub>-MCC composite was completed  
 243 after 8 hours.

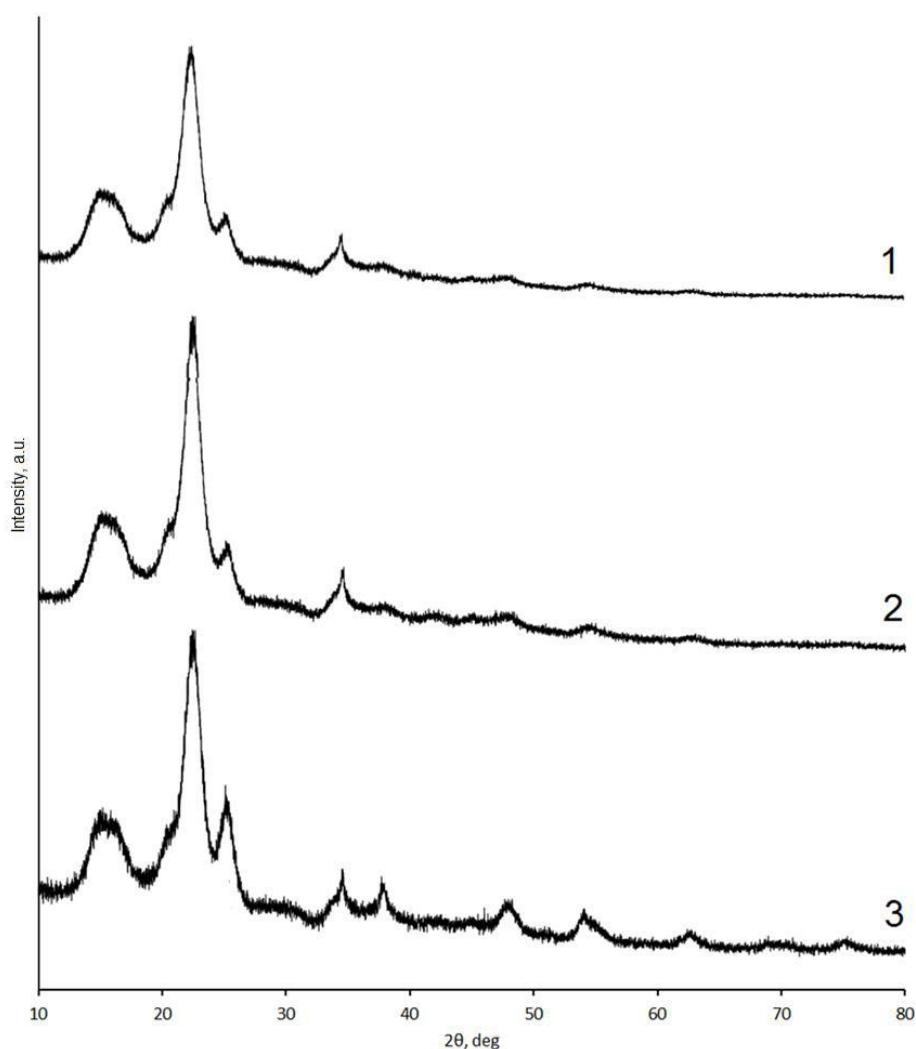
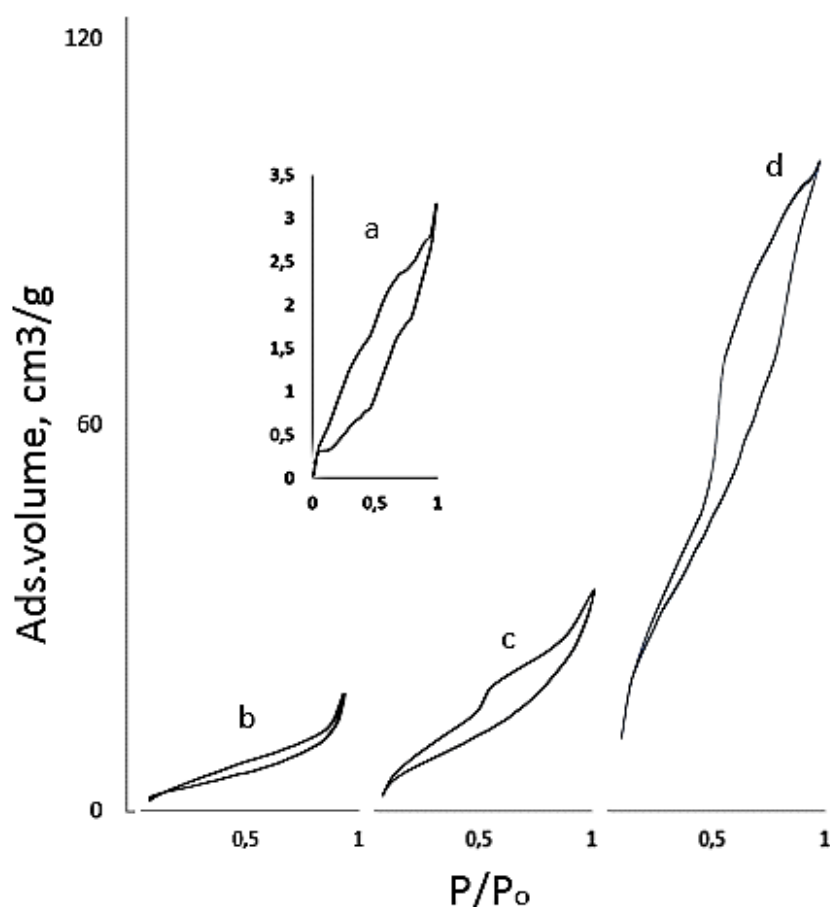


**Figure 6.** X-ray diffraction data of TiC5 (1), TiC6 (2), TiC3 (3).

According to TEM images in Fig. 8, the synthesis is accompanied by loosening of MCC grains in course of the anatase immobilization. This process is accompanied by a partial cellulose degradation, which was confirmed by nitrogen sorption/desorption data. The surface area, pore volume, and pore diameter of TiC samples with different titania contents and those of the reference Aeroxide P25 TiO<sub>2</sub> are summarized in Table 2. These parameters suggest high adsorption activity of samples TiC1, TiC3, and, especially, TiC4. The isotherms evaluated for MCC-TiO<sub>2</sub> composites were classed with type IV and V isotherms, suggesting the micro- and mesoporous character of the samples. For sample TiC4, the amount of nitrogen adsorbed rapidly increases at all relative pressures, reaching 95 cm<sup>3</sup>/g (Fig. 7d). The pore size distribution for sample TiC4 has a single narrow peak indicating that this sample is highly homogeneous.

259 Isotherms and pore radius distributions for samples TiC1 and TiC3 have the  
 260 similar shape, but the amount of adsorbed nitrogen is different [for TiC1, the  
 261 amount is 20 cm<sup>3</sup>/g (Fig. 7b), and for TiC3, the amount is 40 cm<sup>3</sup>/g (Fig. 7c)]. For  
 262 initial MCC the amount of nitrogen adsorbed is comparatively low – near 3 cm<sup>3</sup>/g,  
 263 and pore size distribution was wide with several different predominant pore sizes  
 264 (See Figure S8. Supporting Information). As one can see in the course of  
 265 synthesis the pore size distribution became narrow. It supported the assumption,  
 266 that reaction of cellulose and titanium isopropoxide goes especially at amorphous  
 267 regions.



268  
 269 **Figure 7.** N<sub>2</sub> adsorption/desorption isotherms for MCC (a), TiC1 (b), TiC2 (c), and  
 270 TiC4 (d).

271  
 272 The specific surface area of TC samples proportionally increases with the increase  
 273 of titania content, which is characteristic of particles undergoing insignificant  
 274 coarsening. The mean size of TC series crystalline particles, calculated by  
 275 Scherrer equation from curves 3 and 4 (Fig. 3) and curve 3 (Fig. 6) was about 30  
 276 nm.

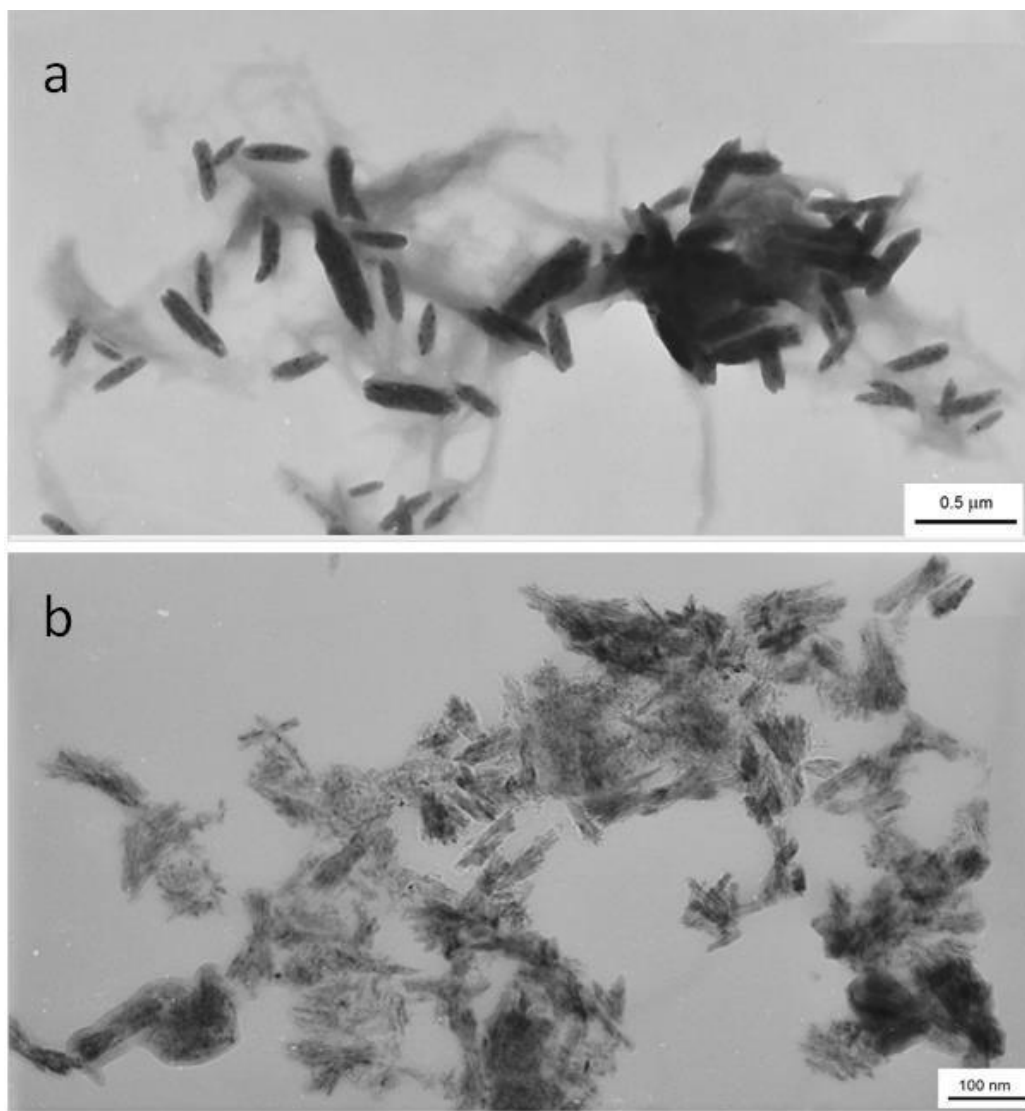


**Figure 8.** TEM micrographs of MCC (a) and TiC4 (b) samples.

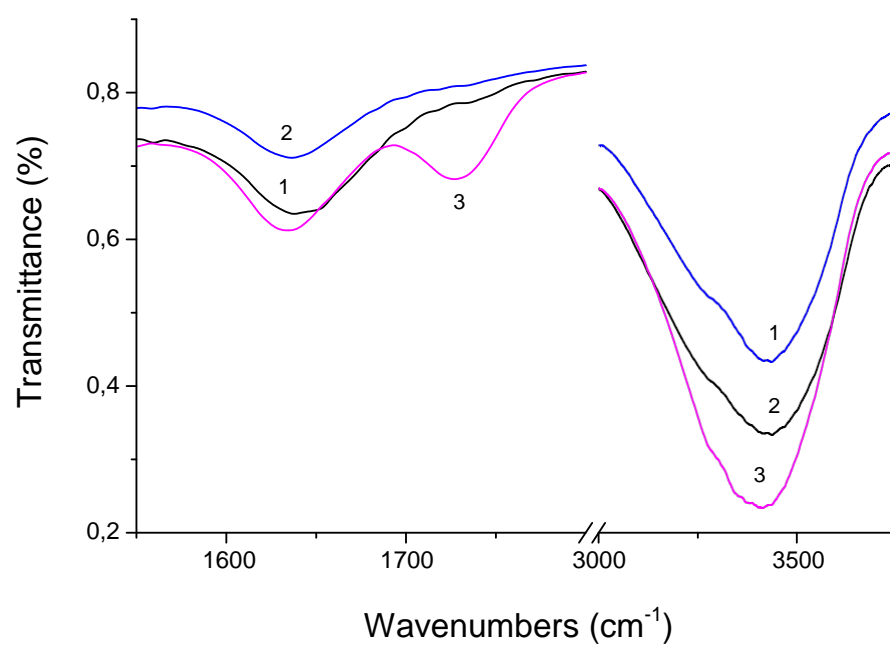
At the same time, during the formation of MCC-TiO<sub>2</sub> composite, the degree of crystallinity of cellulose increases from 91% (pure MCC) to 98% (TiC4) with an increase in the concentration of titanium dioxide. This can be explained by the fact that the reaction between the components (Equations 1-4) proceeds primarily through the most accessible and active groups located in the amorphous regions. The data on crystallinity of cellulose were obtained by Segal method [Segal et al. 1959; Yacenko et al. 2019]. For more details, see Supporting Information.



**Table 2.** Area, average pore radius and pore volume of samples with different titania content (TiC1, TiC2, TiC3, TiC4) and Aeroxide P25 TiO<sub>2</sub>.

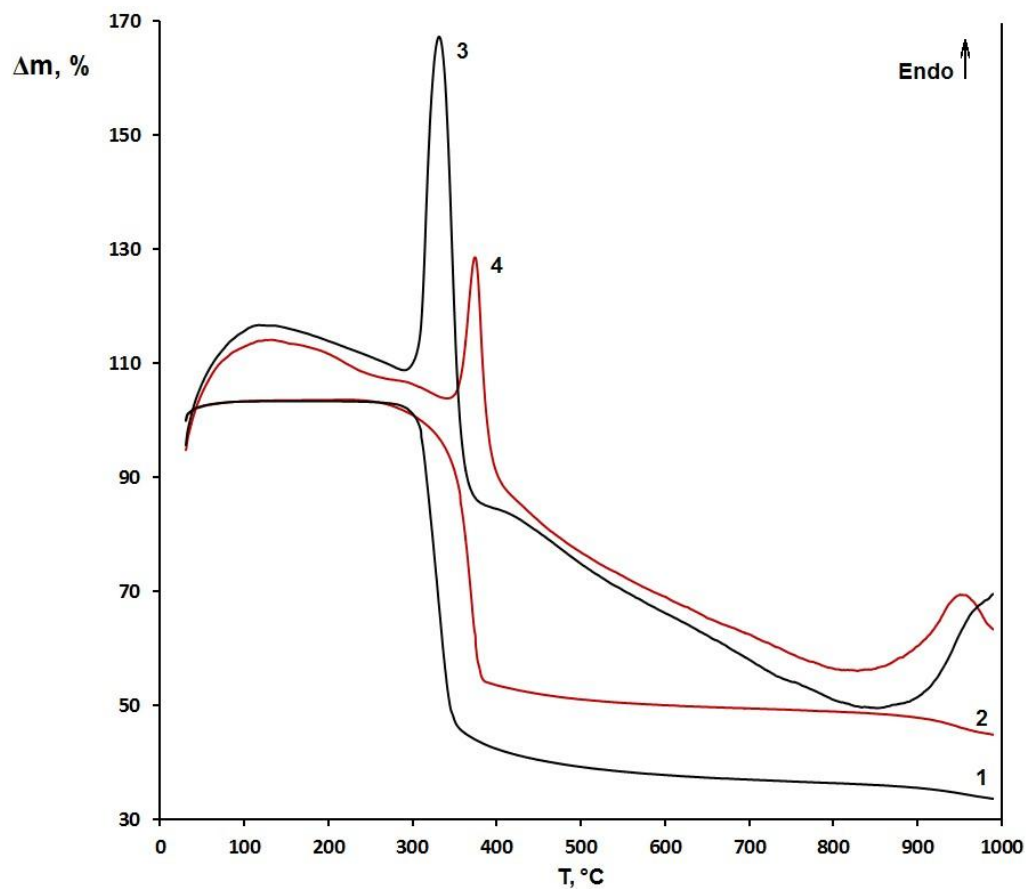
Sample	Specific surface area, m <sup>2</sup> /g	Average pore diameter, Å	Pore volume, cm <sup>3</sup> /g
MCC	2.5	21	0.004
TiC1	10.2	<16	0.018
TiC3	27.4	17.7	0.037
TiC4	55.0	19.5	0.060
Aeroxide P25 TiO <sub>2</sub>	50.9	16	0.12

The formation of anatase TiO<sub>2</sub>-MCC composites was also confirmed by FTIR spectroscopy and thermal analysis. An example of pure cellulose MCC and composite TiC4 sample with the highest titania content (see Table 1) is given in Fig 9. The strong IR band of hydroxyl bending vibrations in cellulose at 1630 cm<sup>-1</sup> was observed to shift to lower frequencies upon the composite formation, down to 1620 cm<sup>-1</sup> in TiC4, suggesting strong interfacial interaction between hydroxy groups of MCC and cations of titania nanoparticles. In the case of TiD sample this shift in IR spectrum was not observed. The same conclusion can be drawn from the shift of the stretching vibration band of cellulose hydroxyls at 3430 cm<sup>-1</sup> to lower frequencies: 3410 cm<sup>-1</sup> in the composite material (Fig. 9). The TG-DSC analysis indicated a progressive decomposition of cellulose with an increase of temperature, accompanied by a release of different gaseous products including hydrogen, methane, carbon monoxide, etc. The thermolysis process in argon atmosphere is characterized by endothermic peaks of DSC curves. The results in Fig. 10 show that the main endothermic peak of MCC was shifted to higher temperatures by 42 °C in TiC4 composite while its magnitude was decreased from 1.32 mW/mg to 0.57 mW/mg. This confirms a tight coupling between the two components of the composite. The ~50% weight loss in the temperature range of thermolysis, observed in TiC4 compared with MCC, validates the presence of stable inorganics.



313

314 **Figure 9.** IR spectra of MCC (1), TiD1 (2) and TiC4 (3) samples.

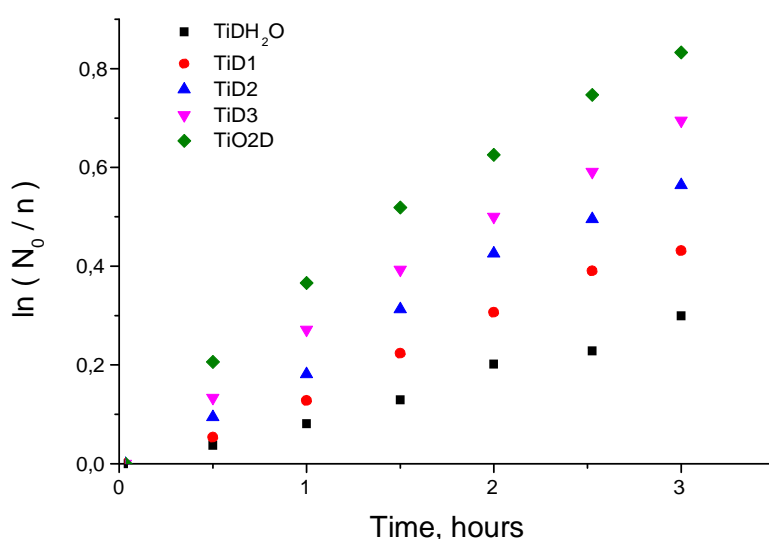


315

316 **Figure 10.** TG (1, 2) and DSC (3, 4) analyses of MCC (1, 3) and TiC4 (2, 4) samples under argon  
317 atmosphere.

318

319 In the photocatalytic experiments, formic acid was used as a model pollutant not  
 320 sensitive to UVA radiation, which favorably distinguishes it from commonly used  
 321 dyes rhodamine and methylene blue. The kinetics of the formic acid degradation  
 322 is shown in Figs 12 and 13 in a semi-logarithmic frame, which evidences the first  
 323 order decomposition kinetics, far from saturation phenomena. The photocatalytic  
 324 rate constants in Table 1 were obtained from the linear least-squared fits of the  
 325 experimental data. The kinetics observed with TD samples was relatively slow  
 326 (Fig. 11). The thermal post-treatment (TiO<sub>2</sub>D sample) did not significantly  
 327 enhance the material activity, which remained much slower compared to that of  
 328 commercial TiO<sub>2</sub> P25 photocatalysts. This correlates with our XRD measurements  
 329 shown poor crystallization of anatase TiO<sub>2</sub> in the n-decane synthesis conditions.  
 330 In contrast, TC samples synthesized in caproic acid exhibited an appreciably faster  
 331 kinetics (Fig. 12) corresponding to their higher photocatalytic activity; among  
 332 these samples, TiC4 prepared with the highest titania content possessed the highest  
 333 activity. We notice that because of a steric factor, the hydroxy group at C-  
 334 6 carbon atom of cellulose is expected to be most active in the titania attraction.  
 335 Because of this, the effective amount of anatase in the composite material cannot  
 336 exceed a limit imposed by the cellulose content, which is expected to be about 50  
 337 wt%. Apparently, this limit is attained in TiC4 sample and further increase of the  
 338 titania content is inappropriate.



339  
 340 **Figure 11.** Kinetics of formic acid decomposition under UV irradiation in aqueous solutions using  
 341 TiDH<sub>2</sub>O, TiD1, TiD2, TiD3 and TiO<sub>2</sub>D photocatalysts.

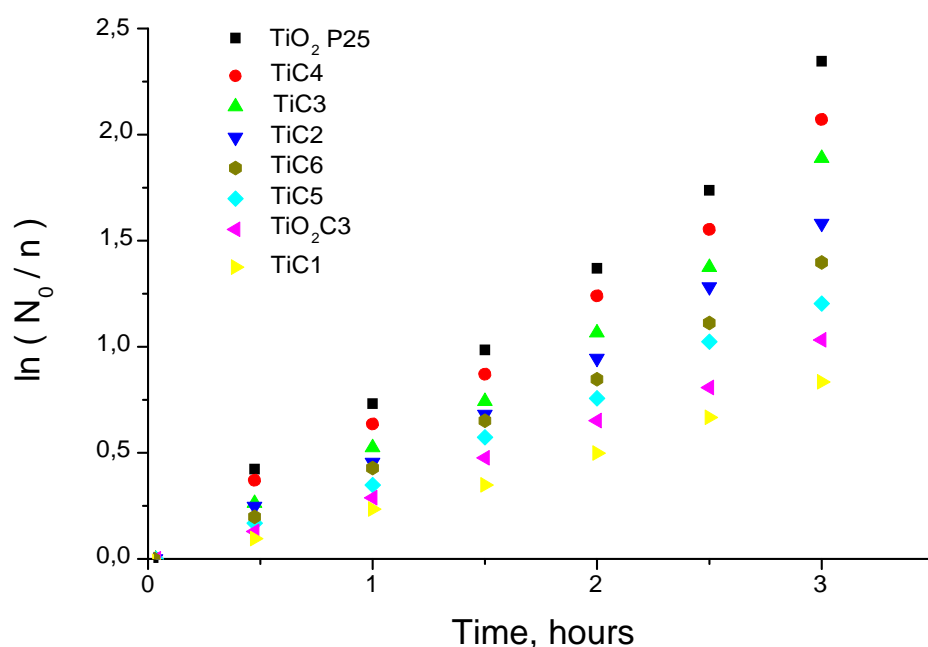
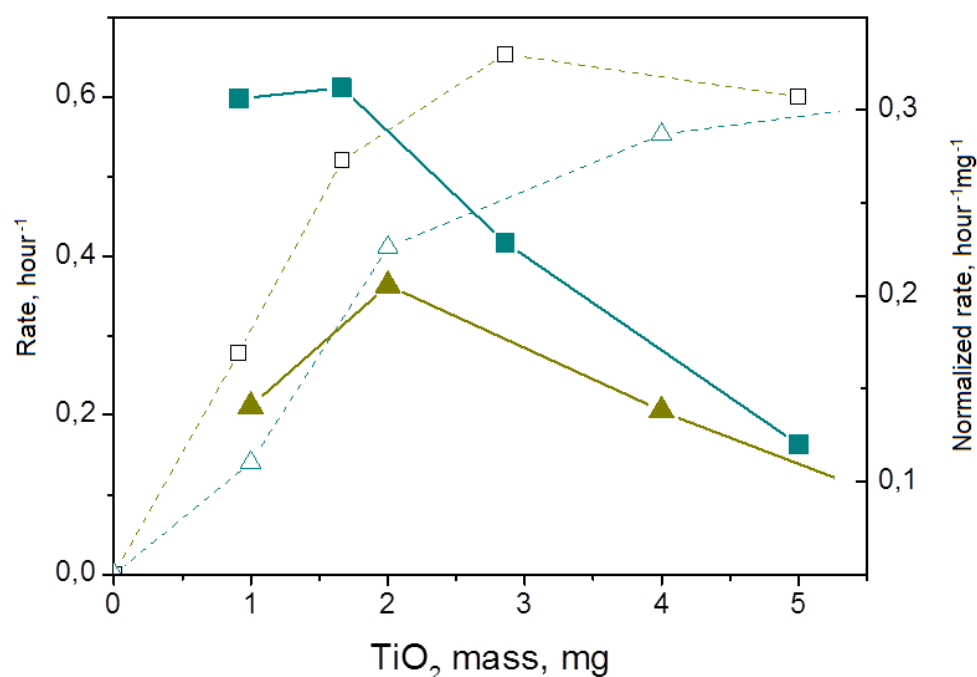


**Figure 12.** Kinetics of formic acid decomposition under UV irradiation in aqueous solutions using TiC1, TiC2, TiC3, TiC4, TiC5, TiC6, TiO<sub>2</sub>C3 and TiO<sub>2</sub> P25 photocatalysts.

A deeper comparison between our best prepared and reference TiO<sub>2</sub> P25 photocatalysts can be performed based on the intrinsic efficiency  $\gamma$  defined as the conversion yield of an absorbed photon to a chemical reaction. This is an important characteristic showing potentiality of the material application in the photocatalytic process. It can be shown that for a relatively small mass and first order process kinetics,  $\gamma$  is proportional to the reaction rate constant  $R$  normalized on the photocatalyst mass [Cheng et al. 2018; Bouslama et al. 2012]. This normalized rate reflects the material effectiveness when the photocatalyst mass is relatively small and decreases at the larger masses due to the saturation of light absorbance in accordance with the Beer-Lambert law. Our first order kinetics permits this comparison of the material activities. Fig. 12 shows reaction rates and normalized reaction rates of the best composite materials of TiC series in comparison with the reference TiO<sub>2</sub> P25. These rates, reported in Table 1, were obtained from the slopes of the experimental data presented in semi-logarithmic frame of  $\ln(C_0/C)$  versus time of UVA illumination. As expected, the decomposition rate increases with an increase of the photocatalyst mass in both TC and TiO<sub>2</sub> P25 materials because of an increased light absorbance, and saturates when UVA lamp power is totally absorbed by the material. The

364 saturation rates of both types of materials were found similar. Similarly, both TC  
 365 and TiO<sub>2</sub> P25 materials reached the maximal normalized rates (on photocatalyst  
 366 mass) at the same TiO<sub>2</sub> loadings, apparently indicating similar effectiveness in  
 367 screening the UVA lamp photons related to the morphology factors (specific  
 368 surface area and particle size of titania component). However, values of the  
 369 maximum normalized rates were different and that of TC photocatalysts was  
 370 almost two times higher compared to TiO<sub>2</sub> P25. The higher intrinsic efficiency ( $\gamma$ )  
 371 of TC composites could not be an explanation, since absolute rates at infinite  
 372 photocatalyst mass of TC and reference materials were similar (Fig. 13). In  
 373 contrast, finer granulometry of TC composite particles could be a reason. Indeed  
 374 large agglomerates of TiO<sub>2</sub> P25 particles (practically of size above 100 nm)  
 375 possess a significant screened volume, not accessible by UV lamp photons; as a  
 376 result, this material has a significant mass, which is excluded from the  
 377 photocatalytic process. In contrast, the TC component, which strongly scatter and  
 378 not absorbed UVA light [Lu et al. 2013], effectively increase the residence time of  
 379 UVA photons in the reaction volume; the longer interaction time creates  
 380 conditions for a more efficient light energy deposition into the photocatalyst.



381  
 382 **Figure 13.** Absolute (□, △) and normalized on photocatalyst mass (■, ▲) decomposition rates of  
 383 formic acid observed with TC (□, ■) and TiO<sub>2</sub> P25 (△, ▲) photocatalysts.

## 384 Conclusion

385 In this work, novel cellulose-TiO<sub>2</sub> composite photocatalysts were synthesized via  
386 solvothermal method in order to assemble microcrystalline organic cellulose and  
387 inorganic titania components. Two series of materials were prepared in n-decane  
388 and caproic acid solvents. In n-decane, the synthesis resulted in a poor  
389 crystallization of anatase titania and the subsequent thermal post treatment  
390 destroyed the composites. In contrast, in caproic acid, acting as solvent and  
391 reagent, anatase TiO<sub>2</sub> nanoparticles were formed onto the crystalline domains of  
392 cellulose. Strong covalent bonds between the organic and inorganic components  
393 of the composite were evidenced by IR spectroscopy, <sup>1</sup>H NMR and TG/DSC  
394 methods. The photocatalytic activity of the synthesized materials was evaluated by  
395 the decomposition of formic acid in aqueous solutions under UVA lamp  
396 illumination and compared with that of reference photocatalyst Aeroxide P25  
397 TiO<sub>2</sub>. The absolute activities of composites and reference photocatalyst were  
398 similar. On the other hand, much smaller titania mass was required in order to  
399 reach the maximum activity in the prepared composites compared to the reference  
400 photocatalyst. This effect was attributed to the organic component, which  
401 effectively scatters UVA lamp photons, thus increasing efficiency of the light  
402 energy deposition into the inorganic anatase TiO<sub>2</sub> component.

403 **Acknowledgments.** Authors are grateful to Ministry of Science and Higher Education of Russian  
404 Federation for financial support (Project No 0097-2019-0017).

## 405 References

- 406 Bouslama M, Amamra MC, Jia Z, Ben Amar M, Brinza O, Chhor K, Abderrabba M, Vignes  
407 JL, Kanaev A (2012) Nanoparticulate TiO<sub>2</sub>-Al<sub>2</sub>O<sub>3</sub> photocatalytic media: effect of particle size and  
408 polymorphism on photocatalytic activity. ACS Catal 2:1884–1892; doi:10.1021/cs300033y
- 409 Brandes R, Souza L, Vargas V, Oliveira E, Mikowski A, Carminatti C, Al-Qureshi H,  
410 Recouvreux D (2016) Preparation and Characterization of Bacterial Cellulose/TiO<sub>2</sub> Hydrogel  
411 Nanocomposite. Journal of Nano Research 43:73–80;  
412 doi:10.4028/www.scientific.net/JNanoR.43.73
- 413 Butman MF, Ovchinnikov NL, Karasev NS, Kochkina NE, Agafonov AV, Vinogradov AV  
414 (2018) Photocatalytic and adsorption properties of TiO<sub>2</sub>-pillared montmorillonite obtained by  
415 hydrothermally activated intercalation of titanium polyhydroxo complexes. Beilstein J.  
416 Nanotechnol 9:364–378; doi:10.3762/bjnano.9.36

Cardoso GV, Mello LR, Zanatta P, Cava S, Raubach CW, Moreira ML (2018) Physico-chemical description of titanium dioxide–cellulose nanocomposite formation by microwave radiation with high thermal stability. *Cellulose* 25:2331–2341; doi:10.1007/s10570-018-1734-2

Cheng K, Chhor K, Passarello JP, Colbeau-Justin C, Kanaev A (2018) Photocatalytic nanoparticulate  $Zr_xTi_{1-x}O_2$  coatings with controlled homogeneity of elemental composition. *Chemistry Select* 3:11118–11126; doi:10.1002/slct.201801732

Dette C, Pérez-Osorio MA, Kley CS, Punke P, Patrick CE, Jacobson P, Guistino F, Jung SJ, Kern K (2014)  $TiO_2$  anatase with a bandgap in the visible region. *Nano Lett* 12:6533–6538; doi: 10.1021/nl503131s

Farag S, Amr A, El-Shafei A, Ibrahim HM, Asker MS (2017) Influence of bacterial cellulose for synthesis and application of titanium dioxide nanoparticles compared with sol-gel method. Proceedings of 60th The IRES International Conference, Munich, Germany 15-23

Filippo E, Carlucci C, Capodilupo AL, Perulli P, Conciauro F, Corrente GA, Gigli G, Ciccarella G (2015) Enhanced photocatalytic activity of pure anatase  $TiO_2$  and Pt- $TiO_2$  nanoparticles synthesized by green microwave assistant route. *Mater. Res* 18:473; doi:10.1590/1516-1439.301914

French AD (2014) Idealized powder diffraction patterns for cellulose polymorphs. *Cellulose* 21:885-896; doi: 10.1007/s10570-013-0030-4

Galkina OL, Sycheva A, Blagodatskiy A, Kaptay G, Katanaev VL, Seisenbaeva GA, Kessler VG, Agafonov AV (2014) The sol-gel synthesis of cotton/ $TiO_2$  composites and their antibacterial properties. *Surface & Coatings Technology* 253:171–179; doi:10.1016/j.surfcoat.2014.05.033

Garusinghe UM, Raghuwanshi VS, Batchelor W, Garnier G (2018) Water resistant cellulose-titanium dioxide composites for photocatalysis. *Sci Rep* 8:2306; doi:10.1038/s41598-018-20569-w

Gorbovyi P, Uklein A, Tieng S, Traore M, Chhor K, Museur L, Kanaev A (2011) Novel nanostructured pHEMA-(oxo) $TiO_2$  hybrid materials with efficient light-induced charge separation, *Nanoscale* 3:1807–1812; doi: 10.1364/OME.3.000533

Habibi S, Jamshidi M (2020) Synthesis of  $TiO_2$  nanoparticles coated on cellulose nanofibers with different morphologies: Effect of the template and sol-gel parameters. *Mater. Sci. in Semiconductor Processing* 109:104927; doi:10.1016/j.mssp.2020.104927

He D, Li Y, Wang J, An Q (2016) Tunable nanostructure of  $TiO_2$  reduced oxide composite for high photocatalysis. *Applied Microscopy* 46:37–44; doi:10.9729/AM.2016.46.1.37

Ioelovich M. (2014) *Cellulose: Nanostructured natural polymer*. Saarbrücken: Lap Lamber Acad, 100.

Kaseem M, Hamad K, Rehman ZU (2019) Review of Recent Advances in Poly(lactic Acid)/ $TiO_2$  Composites. *Materials* 12:3659; doi:10.3390/ma12223659

Kayaalp M, Rathousk J, Bein T (2014) Tailoring the morphology of mesoporous titania thin film through biotemplating with nanocrystalline cellulose. *J. Am. Chem. Soc* 136:5930–5937; doi:10.1021/ja411292u

Khalid A, Ullah H, Ul-Islam M, Khan R, Khan S, Ahmad F, Khal T, Wahid F (2017) Bacterial cellulose– $TiO_2$  nanocomposites promote healing and tissue regeneration in burn mice model. *RSC Adv* 7:47662–47668; doi:10.1039/c7ra06699f

458 Kuznetsov AI, Kameneva O, Biturin N, Rozes L, Sanchez C, Kanaev A. (2009) Light-  
459 induced photopatterning of organic-inorganic TiO<sub>2</sub> based hybrid materials with tunable interfacial  
460 electron transfer, *Phys. Chem. Chem. Phys* 11:1248–1257; doi: 10.1039/B814494J

461 Li Y, Zhang JC, Kong F, Li W, Yang C, Hsiao BS (2020) Facile synthesis of TiO<sub>2</sub>/CNC  
462 nanocomposites for enhanced Cr(VI) photoreduction: Synergistic roles of cellulose nanocrystals.  
463 *Carbohydr. Polym* 233:115838; doi: 10.1016/j.carbpol.2020.115838

464 Lu Y, Sun Q, Liu T, Yang D, Liu Y, Li J (2013) Fabrication, characterization and  
465 photocatalytic properties of millimeter-long TiO<sub>2</sub> fiber with nanostructures using cellulose fiber as  
466 a template. *J. Alloys Compd* 577:569–574; doi:10.1016/j.jallcom.2013.06.183

467 Luo Y, Xu J, Huang J (2014) Hierarchical nanofibrous anatase-titania–cellulose composite  
468 and its photocatalytic property. *CrystEngComm* 14:464–471; doi:10.1039/c3ce41906a

469 Melvin NHK, Leo CP (2019) The coherence between TiO<sub>2</sub> nanoparticles and microfibrillated  
470 cellulose in thin film for enhanced dispersal and photodegradation of dye. *Progress in Organic*  
471 *Coatings* 132:70–75; doi:10.1016/j.porgcoat.2019.02.017

472 Morawski AW, Kusiak-Nejman E, Przepiórski J, Kordala R, Pernak J (2013) Cellulose-TiO<sub>2</sub>  
473 nanocomposite with enhanced UV–Vis light absorption. *Cellulose* 20:1293–  
474 1300; doi:10.1007/s10570-013-9906-6

475 Morshed MN, Azad SA, Deb H, Shaun BB, Shen XL (2020) Titania-loaded cellulose-based  
476 functional hybrid nanomaterial for photocatalytic degradation of toxic aromatic dye in water. *J. of*  
477 *Water Process Engineering* 33:101062; doi: 10.1016/j.jwpe.2019.101062

478 Mory K (2005) Photo-functionalized materials using g nanoparticles: photocatalysis. *KONA*  
479 *Powder Part J* 23:205–214; doi:10.14356/kona.2005023

480 Oliveira AC, Santos MS, Brandão LMS, Resende ITF, Leo IM, Morillo ES, Yerga RMN,  
481 Fierro JLG, Egues SMS, Figueiredo RT (2017) The effect of cellulose loading on the photoactivity  
482 of cellulose-TiO<sub>2</sub> hybrids for hydrogen production under simulated sunlight. *International Journal*  
483 *of Hydrogen Energy* 42:28747–28754; doi:10.1016/j.ijhydene.2017.09.022

484 Postnova I, Kozlova E, Cherepanova S, Tsybulya S, Rempel A, Shchipunov Y (2015) Titania  
485 synthesized thorough regulated mineralization of cellulose and its photocatalytic activity. *RSC*  
486 *Adv* 5:8544–8551; doi:10.1039/C4RA15862H

487 Rahmawati F, Fadillah M, Mudjijono I (2017) Composite of Nano-TiO<sub>2</sub> with Cellulose  
488 Acetate Membrane from Nata de Coco (Nano-TiO<sub>2</sub>/CA(NDC)) for Methyl Orange Degradation *J.*  
489 *Mater. Environ. Sci* 8:287–297

490 Sathasivam S, Bhachu SD, Li Y, Chadwick N, Althabaiti SA, Alyobi AO, Basahel SN,  
491 Carmalt CJ, Parkin IP (2015) Tungsten doped TiO<sub>2</sub> with enhanced photocatalytic and opt-  
492 electrical properties via aerosol assisted chemical vapor deposition. *Sci. Rep* 4:10952–10956;  
493 doi:10.1038/srep10952

494 Segal L, Creely JJ, Martin AE, Contrad CM (1959) An Empirical method for estimating the  
495 degree of crystallinity of native cellulose using the X-ray diffractometer. *Text Res J* 29(10):786-  
496 794; doi: 10.1177/004051755902901003

497 Shahrezaei M, Habibzadeh S, Babaluo AA, Hosseinkhani H, Haghighi M, Hasanzedah A,  
498 Tahmasebpour R (2017) Study of synthesis parameters and photocatalytic activity of TiO<sub>2</sub>



nanostructures J. Exp. Nanosci 12:45; doi:10.1080/17458080.2016.1258495  
 Sharon M, Modi F, Sharon M (2016) Titania based nanocomposite as a photocatalyst: A  
 review. AIMS Materials Science 3:1236-1254; doi:10.3934/matricsci.2016.3.1236  
 Shevtsova TA, Zlotski SV (2018) Facile sol-gel synthesis of metal oxide nanoparticles in a  
 cellulose paper template. Doklady Bguir 112:113–115  
 Sirvio JA, Visanko M, Heiskanen JP, Liimatainen H (2016) UV-absorbing cellulose  
 nanocrystals as functional reinforcing fillers in polymer nanocomposite films. J. Mater. Chem. A  
 4:6368–6375; doi:10.1039/C6TA00900J  
 Sun D, Yang J, Wang X (2010) Bacterial cellulose/TiO<sub>2</sub> hybrid nanofibers prepared by the  
 surface hydrolysis method with molecular precision. Nanoscale 2:287–292;  
 doi:10.1039/b9nr00158a  
 Tang B, Chen H, Peng H, Wang Z, Huang W (2018) Graphene Modified TiO<sub>2</sub> Composite  
 Photocatalysts: Mechanism, Progress and Perspective. Nanomaterials 8:105;  
 doi:10.3390/nano8020105  
 Tieng S, Kanaev A, Chhor K (2011) New homogeneously doped Fe(III)–TiO<sub>2</sub> photocatalyst  
 for gaseous pollutant degradation. Appl. Cat. A 399:191–197; doi:10.1016/j.apcata.2011.03.056  
 Wang SB, Pan L, Song JJ, Mi W, Zou JJ, Wang L, Zhang X (2015) Titanium-defected  
 undoped anatase TiO<sub>2</sub> with p-type conductivity, room-temperature ferromagnetism, and  
 remarkable photocatalytic performance. J. Am. Chem. Soc 137:2975–2983;  
 doi:10.1021/ja512047k  
 Wang W, Wang J, Shi X, Yu Z, Song Z, Dong L, Jiang G, Han S (2016) Synthesis of  
 Mesoporous TiO<sub>2</sub> Induced by NanoCellulose and Its Photocatalytic Properties. BioResources 11:  
 3084–3093; doi: 10.15376/biores.11.2.3084–3093  
 Wittmar A, Thierfeld H, Köcher S, Ulbricht M (2015) Routes towards catalytically active  
 TiO<sub>2</sub> doped porous cellulose. RSC Adv 5:35866–35873; doi:10.1039/C5RA03707G  
 Xiao H, Li J, He B (2017) Anatase-Titania Templated by Nanofibrillated Cellulose and  
 Photocatalytic Degradation for Methyl Orange. J. Inorg. and Organomet. Polym. Mater 27:1022–  
 1027; doi: 10.1007/s10904-017-0550-8  
 Yatsenko DA, Medvedeva TB (2019) Estimating crystallinity index of microcrystalline cellulose  
 using diffraction methods. Journal of Structural Chemistry 60:1430–1436; doi:  
 10.1134/S0022476619090075  
 Zdravkov A, Kudryashova J, Kanaev A, Povolotskiy A, Volkova A, Golikova E, Khimich N  
 (2015) A new solvothermal route to efficient titania photocatalyst. Mater. Chem. Phys 160:73–79;  
 doi:10.1016/j.matchemphys.2015.04.008  
 Zhang X, Chen YL, Liu RS, Tsai DP (2013) Plasmonic photocatalysis, Rep. Prog. Phys 76:  
 046401; doi: 10.1088/0034-4885/76/4/046401  
 Zlotski SV, Uglov VV (2017) Facile sol-gel synthesis of metaloxide nanoparticles in a  
 cellulose paper template J. Nanomedicine Nanotechnology S8:002; doi: 10.4172/2157-7439.S8-  
 002



[Click here to access/download  
Supplementary Material  
SI\\_Khimich\\_Revision\\_2.docx](#)

